中國機械工程學刊第四十卷第六期第 605~616 頁(民國一百零八年)
Journal of the Chinese Society of Mechanical Engineers, Vol.40, No.6, pp 605~616(2019)

Coupled Micro-vibrations Analysis of a Reaction Wheel Assembly with Flexible Structure

Xiong-Fei Li *and Wei Cheng **

Keyword: micro-vibrations, reaction wheel assembly, substructure method, flexible structure.

ABSTRACT

This paper investigates the coupled micro-vibrations between a reaction wheel assembly (RWA) and a flexible structure. Firstly, the Lagrange's energy method is employed to develop vibration equation of the RWA. The RWA model is described by twelve-dof linear differential equation with gyroscopic term. Secondly, based on the established vibration equation, disturbance model of the RWA with a discrete flexible structure is obtained. This disturbance model is simulated and discussed by taking a six-dof system as the study object. Thirdly, a frequency domain substructure method (FDSM) is used to calculate coupled disturbance response of the RWA with a continuous flexible structure, which is designed as analog of the satellite flexible installation interface. The dynamic response is validated by numerical and finite element simulations. The coupled disturbance analysis method involved in this project will provide a theoretical basis for prediction of the coupled disturbance of RWA with satellite flexible interface.

INTRODUCTION

Development of high-precision observation satellite is currently an important topic, also is the inevitable trend in the development of space technology. Therefore, during the design process of satellite, more stringent standards for the satellite platform stability are put forward (Remedia et al., 2015). However, micro-vibrations of satellite, which are characterized by low amplitude and wide frequency band, can seriously degrade the satellite platform stability, and significantly influence imaging quality and pointing accuracy of the satellite (Chen et al., 2016). Satellite micro-vibrations are usually caused by moving parts on-board the satellite, such as reaction wheel assembly (RWA), control moment gyroscope (CMG), cryo-cooler assembly (CCA), camera shutter assembly (CSA) and solar array drive assembly (SADA), which in this situation are termed as micro-vibration sources. Among these moving parts, RWA and CMG are always regarded as the most prominent disturbance sources (Li et al., 2016; Zhang et al., 2010).

RWA are commonly used as actuators of attitude control in satellite. RWA provides control torque for satellite via adjusting rotational acceleration of the high speed rotary flywheel. The rotary flywheel also produces adverse vibrations while providing control torque. Disturbances caused by RWA result primary from the following four factors: flywheel mass imbalance, internal resonance, imperfection in mechanical bearings and motor ripple (Li et al., 2014), in which flywheel mass imbalance is almost considered as the major factor. Masterson et al. (2002) assumed RWA disturbance caused by the flywheel mass imbalance consists of a series of harmonics at discrete frequencies with amplitude proportional to square of the flywheel speed. Internal resonance occurs when the disturbance harmonics cross structural modes. Masterson (1999) developed a four-dof linear flywheel analytical model with radial translational and rock vibrations, which captures the dynamic interaction between structural modes and inertia properties of the flywheel and gyroscopic stiffening effects. In this paper, the RWA model is considered as a twelve-dof linear vibration system which takes vibration of the frame into account. Vibration equation of the system is developed by the Lagrange's energy method.

RWA micro-vibrations extremely easily to happen dynamic couple with the flexible satellite installation interface. The RWA disturbances induce vibrations in the satellite and excite its flexible modes.

Paper Received September, 2018. Revised July, 2019, Accepted August, 2019, Author for Correspondence: Xiong-Fei Li.

* *Ph. D student, Department of Aeronautic Science and Engineering, Beihang University, Beijing 100083, China.*

** *Professor, Department of Aeronautic Science and Engineering, Beihang University, Beijing 100083, China.*

The satellite vibrations subsequently drive the RWA and create additional disturbances, and this makes the RWA micro-vibrations more complex. The coupling characteristics between RWA and flexible satellite interface are complicated and will increasingly deteriorate point performances of the satellite (Narayan et al., 2008). Thus, with the development of high-precision observation satellite, study of coupled micro-vibrations characteristics between RWA with flexible structure is of great significance. There has been several researches focusing on investigate these coupled micro-vibrations. Elias et al. (2003) presented a traditional coupling disturbance analysis method, which directly applies the RWA hard-mounted testing spectrums to a spacecraft FRF to predict its performance. They also pointed out that this analysis method could bring a lager error when the internal elastic needs to be considered in the RWA model. To reduce the error caused by ignoring the internal elastic, Elias et al. (1999) and Elias et al. (2002) proposed a coupled disturbance analysis method based on dynamic mass measurement techniques. This method uses a correction term to correct the RWA hard-mount test spectrums, and then applies the corrected spectrums to a spacecraft FRF to predict its performance. This method makes a better correction effect in most frequency band, but it is still ineffective in some frequency band. The main cause is measurement of the RWA dynamic mass fails to consider influence of the flywheel gyroscopic effect. Zhou et al. (2011) and Zhang et al. (2013) studied influence of the flywheel gyroscopic effect on the coupling disturbance analysis based on theoretical modeling and experimental measurement. A seismic micro-vibration measurement system was developed to measure the coupled micro-vibrations, and an analytical model of the RWA with the test system was established to analyze the coupled micro-vibrations. The results indicate that the flywheel gyroscopic effect is important and cannot be ignored in the coupling disturbance analysis.

However, the aforementioned researches did not deeply discuss the coupled micro-vibration characteristics of RWA with flexible structure since only a few effective methods exist to model and analyze the coupled micro-vibrations. In this paper, the disturbance modeling methods of a RWA with both a discrete structure and a continuous flexible structure are presented. Taking a six-dof spring-damping-force of mass system as the discrete flexible structure, numerical model and finite element model (FEM) of the coupling system are established, based on which dynamic characteristics of the coupling system are simulated and investigated. Furthermore, the coupled disturbance response of a RWA with a continuous flexible structure is obtained by a frequency domain substructure method (FDSM) and then been validated by numerical and FEM simulations. The coupled disturbance modeling and analysis methods involved in this paper will provide a theoretical basis for prediction of the coupled disturbance of RWA with the satellite flexible installation interface.

VIBRATION EQUATION OF RWA

Description and Simplification of RWA Model

As depicted in Fig. 1, the RWA structure mainly consists of three parts: a flywheel, two bearings and a frame, where the flywheel supported to the frame by a pair of face to face mounted angular ball bearings (Zhou et al., 2012). Defining coordinate $o_0x_0y_0z_0$ (coordinate 0) is the frame-fixed coordinate, where the origin o_0 locates at center of mass (COM) of the frame, and z_0-axis is in line with the flywheel axis. Assuming COMs of the flywheel and frame are coincident at the initial state.

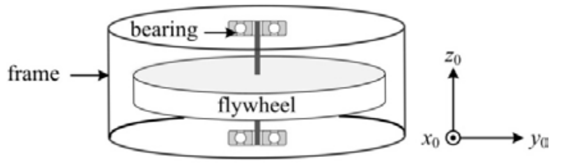

Fig. 1. Schematic diagram of RWA structure.

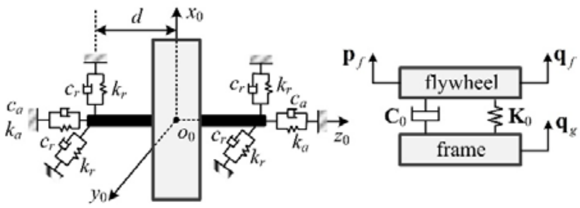

Fig. 2. Equivalent springs model of the bearings.

The flywheel and frame can be considered as six-dof rigid bodies since the flywheel rotary speed is usually far below the critical point. As shown in Fig. 2, all the supporting bearings can be equivalent to linear springs, where k_r and k_a represent radial and axial equivalent stiffness of the bearings, respectively, c_r and c_a represent the equivalent damping, and d is the bearings supporting length. All the equivalent stiffness and damping can be equivalent to the origin o_0 into a six-dof spring that the RWA model can be simplified into a twelve-dof mass-spring-damping system.

The equivalent stiffness and damping matrixes of the six-dof spring are, respectively, defined as:

$$\begin{aligned} \mathbf{K}_0 &= \mathrm{diag}\left[\mathbf{K}_t \quad \mathbf{K}_r\right], \\ \mathbf{C}_0 &= \mathrm{diag}\left[\mathbf{C}_t \quad \mathbf{C}_r\right], \end{aligned} \tag{1}$$

where $\mathbf{K}_t$ and $\mathbf{K}_r$ represent translational and torsional stiffness matrixes of the six-dof spring, respectively, and $\mathbf{C}_t$ and $\mathbf{C}_r$ represent the damping matrixes.

The translational stiffness and damping matrixes can be obtained by linear summation of the equivalent stiffness and damping, which are, respectively, given as:

$$\mathbf{K}_t = \mathrm{diag}\begin{bmatrix}2k_r & 2k_r & 2k_a\end{bmatrix}, \\ \mathbf{C}_t = \mathrm{diag}\begin{bmatrix}2c_r & 2c_r & 2c_a\end{bmatrix}. \tag{2}$$

Taking derivation of the y-axis torsional stiffness as example, calculation of the torsional stiffness matrix is demonstrated. As illuminated in Fig. 3, assuming the flywheel happen a small torsional deformation ε around y-axis, the two x-axis radial springs will generate opposite direction translational transformation Δ_ε, which can be calculated by:

$$\Delta_\varepsilon = d\sin\varepsilon. \tag{3}$$

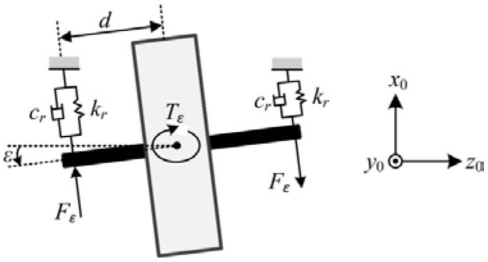

Fig. 3. Equivalent model of y-axis torsional spring.

The reactive forces generated by the two x-axis radial springs are equal in value and opposite in direction. The two reactive forces can be equivalent to the origin o_0 as a torque around y-axis:

$$T_\varepsilon = 2F_\varepsilon d = 2k_r d^2 \sin\varepsilon. \tag{4}$$

For axis rotation of the flywheel about the two radial directions, the rotary angular are quite small, so ε tends to zero. Then, the equivalent torque can be simplified as:

$$T_\varepsilon = 2k_r d^2 \varepsilon. \tag{5}$$

Thus, the equivalent torsional stiffness around y-axis can be obtained as:

$$k_{ry} = T_\varepsilon / \varepsilon = 2k_r d^2. \tag{6}$$

Accordingly, we can obtain the equivalent torsional stiffness around x-axis. The equivalent torsional stiffness around z-axis is zero for the flywheel rotation axis is z-axis. Thus, the equivalent torsional stiffness matrix can be achieved as:

$$\mathbf{K}_r = \mathrm{diag}\begin{bmatrix}2k_r d^2 & 2k_r d^2 & 0\end{bmatrix}. \tag{7}$$

Similarly, we can obtain the equivalent torsional damping matrix as:

$$\mathbf{C}_r = \mathrm{diag}\begin{bmatrix}2c_r d^2 & 2c_r d^2 & 0\end{bmatrix}. \tag{8}$$

Finally, the equivalent stiffness and damping matrixes can be, respectively, achieved as:

$$\mathbf{K}_0 = \mathrm{diag}\begin{bmatrix}2k_r & 2k_r & 2k_a & 2d^2k_r & 2d^2k_r & 0\end{bmatrix}, \\ \mathbf{C}_0 = \mathrm{diag}\begin{bmatrix}2c_r & 2c_r & 2c_a & 2d^2c_r & 2d^2c_r & 0\end{bmatrix}. \tag{9}$$

Vibration Equation of RWA

The Lagrange's energy method is used to develop vibration equation of the RWA (Chen, 1997). General form of the Lagrange's equation is given as:

$$\frac{d}{dt}\left(\frac{\partial T(\mathbf{q},\dot{\mathbf{q}})}{\partial \dot{\mathbf{q}}}\right) - \frac{\partial T(\mathbf{q},\dot{\mathbf{q}})}{\partial \mathbf{q}} + \frac{\partial V(\mathbf{q},\dot{\mathbf{q}})}{\partial \mathbf{q}} + \frac{\partial D(\mathbf{q},\dot{\mathbf{q}})}{\partial \dot{\mathbf{q}}} = \mathbf{p}, \tag{10}$$

where $\mathbf{q}$ and $\mathbf{p}$ are generalized external force and coordinate vectors of the system, respectively, and T, V and D denote the kinetic, potential and dissipation energy.

The translational displacement vectors of the flywheel and frame COMs are, respectively, defined as:

$$\mathbf{q}_{ft}\Big|_{o_0x_0y_0z_0} = \begin{bmatrix}x_f & y_f & z_f\end{bmatrix}^{\mathrm{T}}, \\ \mathbf{q}_{gt}\Big|_{o_0x_0y_0z_0} = \begin{bmatrix}x_g & y_g & z_g\end{bmatrix}^{\mathrm{T}}. \tag{11}$$

The angular displacement vectors of the flywheel and frame COMs are, respectively, defined as:

$$\mathbf{q}_{fr}\Big|_{o_0x_0y_0z_0} = \begin{bmatrix}\alpha_f & \beta_f & \gamma_f\end{bmatrix}^{\mathrm{T}}, \\ \mathbf{q}_{gr}\Big|_{o_0x_0y_0z_0} = \begin{bmatrix}\alpha_g & \beta_g & \gamma_g\end{bmatrix}^{\mathrm{T}}. \tag{12}$$

The translational velocity vectors can be obtained from derivation of the translational displacement vectors:

$$\dot{\mathbf{q}}_{ft}\Big|_{o_0x_0y_0z_0} = \begin{bmatrix}\dot{x}_f & \dot{y}_f & \dot{z}_f\end{bmatrix}^{\mathrm{T}}, \\ \dot{\mathbf{q}}_{gt}\Big|_{o_0x_0y_0z_0} = \begin{bmatrix}\dot{x}_g & \dot{y}_g & \dot{z}_g\end{bmatrix}^{\mathrm{T}}. \tag{13}$$

The angular velocity vectors can be obtained from derivation of the angular displacement vectors:

$$\dot{\mathbf{q}}_{fr}\Big|_{o_0x_0y_0z_0} = \begin{bmatrix}\dot{\alpha}_f & \dot{\beta}_f & \dot{\gamma}_f\end{bmatrix}^{\mathrm{T}}, \\ \dot{\mathbf{q}}_{gr}\Big|_{o_0x_0y_0z_0} = \begin{bmatrix}\dot{\alpha}_g & \dot{\beta}_g & \dot{\gamma}_g\end{bmatrix}^{\mathrm{T}}. \tag{14}$$

Euler angles motions are used to define rigid body rotations of the flywheel and frame (Yuan, 1997), as described in Fig. 4. Three rotations are β, α and γ, respectively, and corresponding rotating axes and rotated coordinates are y_0-axis, x_β-axis, z_α-axis and $o_\beta x_\beta y_\beta z_\beta$, $o_\alpha x_\alpha y_\alpha z_\alpha$, $o_\gamma x_\gamma y_\gamma z_\gamma$.

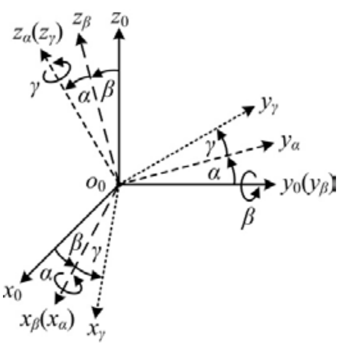

Fig. 4. Euler angles motions of flywheel and frame.

Assuming the flywheel spinning speed is a constant Ω, after the Euler angular motions, angular velocity vectors of the flywheel and frame COMs can be, respectively, expressed in coordinate $o_\alpha x_\alpha y_\alpha z_\alpha$ as:

$$\dot{\mathbf{q}}_{fr}\Big|_{o_\alpha x_\alpha y_\alpha z_\alpha} = \left[\dot{\alpha}_f \quad \dot{\beta}_f \cos\beta_f \quad \Omega - \dot{\beta}_f \sin\beta_f\right]^{\mathrm{T}},$$
$$\dot{\mathbf{q}}_{gr}\Big|_{o_\alpha x_\alpha y_\alpha z_\alpha} = \left[\dot{\alpha}_g \quad \dot{\beta}_g \cos\beta_g \quad \dot{\gamma}_g - \dot{\beta}_g \sin\beta_g\right]^{\mathrm{T}}. \tag{15}$$

Mass matrixes of the flywheel and frame are, respectively, given as follows:

$$\mathbf{M}_f\Big|_{o_0 x_0 y_0 z_0} = \mathrm{diag}\left[m_f \quad m_f \quad m_f\right],$$
$$\mathbf{M}_g\Big|_{o_0 x_0 y_0 z_0} = \mathrm{diag}\left[m_g \quad m_g \quad m_g\right], \tag{16}$$

where m_f and m_g are mass of the flywheel and frame, respectively.

Inertia matrixes of the flywheel and frame are, respectively, given as follows:

$$\mathbf{J}_f\Big|_{o_0 x_0 y_0 z_0} = \mathrm{diag}\left[J_{fr} \quad J_{fr} \quad J_{fz}\right],$$
$$\mathbf{J}_g\Big|_{o_\alpha x_\alpha y_\alpha z_\alpha} = \mathrm{diag}\left[J_{gr} \quad J_{gr} \quad J_{gz}\right], \tag{17}$$

where J_{fr} and J_{gr} are radial inertia of the flywheel and frame, respectively, and J_{fz} and J_{gz} are the polar inertia.

The total kinetic energy T of the system is determined by the following formula:

$$T = \frac{1}{2}\dot{\mathbf{q}}_{ft}^{\mathrm{T}}\mathbf{M}_f\dot{\mathbf{q}}_{ft} + \frac{1}{2}\dot{\mathbf{q}}_{gt}^{\mathrm{T}}\mathbf{M}_g\dot{\mathbf{q}}_{gt} + \frac{1}{2}\dot{\mathbf{q}}_{fr}^{\mathrm{T}}\mathbf{J}_f\dot{\mathbf{q}}_{fr} + \frac{1}{2}\dot{\mathbf{q}}_{gr}^{\mathrm{T}}\mathbf{J}_g\dot{\mathbf{q}}_{gr}. \tag{18}$$

Thus, using Eqs. (13)–(18), the kinetic energy can be obtained as:

$$T = \frac{1}{2}m_f\left(\dot{x}_f^{\,2} + \dot{y}_f^{\,2} + \dot{z}_f^{\,2}\right) + \frac{1}{2}J_{fr}\left[\dot{\alpha}_f^{\,2} + \left(\dot{\beta}_f\cos\beta_f\right)^2\right]$$
$$+\frac{1}{2}J_{fz}\left(\Omega - \dot{\beta}_f\sin\beta_f\right)^2 + \frac{1}{2}m_g\left(\dot{x}_g^{\,2} + \dot{y}_g^{\,2} + \dot{z}_g^{\,2}\right) +$$
$$\frac{1}{2}J_{gr}\left[\dot{\alpha}_g^{\,2} + \left(\dot{\beta}_g\cos\beta_g\right)^2\right] + \frac{1}{2}J_{gz}\left(\dot{\gamma}_g - \dot{\beta}_g\sin\beta_g\right)^2. \tag{19}$$

The elastic displacement and dissipation velocity vectors can be obtained by subtracting the displacement and velocity vectors of the frame from flywheel, respectively, and are expressed as:

$$\mathbf{q}_{\Delta t}\Big|_{o_0 x_0 y_0 z_0} = \left[\mathbf{q}_{gt}^{\mathrm{T}} - \mathbf{q}_{ft}^{\mathrm{T}}\right]^{\mathrm{T}}, \ \mathbf{q}_{\Delta r}\Big|_{o_0 x_0 y_0 z_0} = \left[\mathbf{q}_{gr}^{\mathrm{T}} - \mathbf{q}_{fr}^{T}\right]^{\mathrm{T}},$$
$$\dot{\mathbf{q}}_{\Delta t}\Big|_{o_0 x_0 y_0 z_0} = \left[\dot{\mathbf{q}}_{gt}^{\mathrm{T}} - \dot{\mathbf{q}}_{ft}^{\mathrm{T}}\right]^{\mathrm{T}}, \ \dot{\mathbf{q}}_{\Delta r}\Big|_{o_0 x_0 y_0 z_0} = \left[\dot{\mathbf{q}}_{gr}^{\mathrm{T}} - \dot{\mathbf{q}}_{fr}^{\mathrm{T}}\right]^{\mathrm{T}}. \tag{20}$$

The potential energy and dissipation energy of the system are, respectively, determined by:

$$V = \frac{1}{2}\mathbf{q}_{\Delta t}^{\mathrm{T}}\mathbf{K}_t\mathbf{q}_{\Delta t} + \frac{1}{2}\mathbf{q}_{\Delta r}^{\mathrm{T}}\mathbf{K}_r\mathbf{q}_{\Delta r},$$
$$D = \frac{1}{2}\dot{\mathbf{q}}_{\Delta t}^{\mathrm{T}}\mathbf{C}_t\dot{\mathbf{q}}_{\Delta t} + \frac{1}{2}\dot{\mathbf{q}}_{\Delta r}^{\mathrm{T}}\mathbf{C}_r\dot{\mathbf{q}}_{\Delta r}. \tag{21}$$

Hence, we can obtain the potential energy and dissipation energy of the system by taking Eqs. (2), (7), (8) and (20) into Eq. (21) and are, respectively, expressed as:

$$V = k_r\left[\left(x_f - x_g\right)^2 + \left(y_f - y_g\right)^2\right] + k_a\left(z_f - z_g\right)^2$$
$$+ d^2 k_r\left[(\alpha_f - \alpha_g)^2 + (\beta_f - \beta_g)^2\right],$$
$$D = c_r\left[\left(\dot{x}_f - \dot{x}_g\right)^2 + \left(\dot{y}_f - \dot{y}_g\right)^2\right] + c_a\left(\dot{z}_f - \dot{z}_g\right)^2$$
$$+ d^2 c_r\left[(\dot{\alpha}_f - \dot{\alpha}_g)^2 + (\dot{\beta}_f - \dot{\beta}_g)^2\right]. \tag{22}$$

The generalized external force vector acting on the flywheel is mainly caused by the flywheel mass imbalance, which contains static and dynamic imbalances, as shown in Fig. 5. Static imbalance is caused by offset of the flywheel COM from the rotation axis. Dynamic imbalance is resulted from angular misalignment of principle axis of the flywheel and the rotation axis. When the flywheel rotates, the static and dynamic imbalances will cause imbalances force and torque to the flywheel, which can be equivalent to a force and torque vectors acting on the COM of the flywheel, respectively. The equivalent force and torque vectors are, respectively, expressed as follows:

$$\mathbf{f}_s = \left[U_s\Omega^2\sin(\Omega t + \varphi_s) \quad U_s\Omega^2\cos(\Omega t + \varphi_s) \quad 0\right]^{\mathrm{T}},$$
$$\mathbf{f}_d = \left[U_d\Omega^2\sin(\Omega t + \varphi_d) \quad U_d\Omega^2\cos(\Omega t + \varphi_d) \quad 0\right]^{\mathrm{T}}, \tag{23}$$

where $U_s=m_s r_s$ and $U_d=m_d r_d h_d$ denote the static and dynamic mass imbalances, respectively, and φ_s and φ_d are the initial phases.

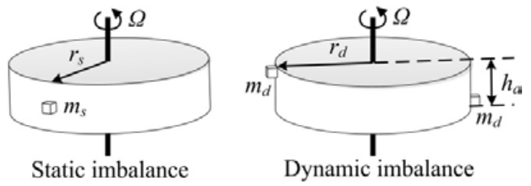

Fig. 5. Static and dynamic imbalances of flywheel.

The generalized external force vector of the system is defined as:

$$\mathbf{p}_R\Big|_{o_0 x_0 y_0 z_0} = \left[\mathbf{f}_f^{\mathrm{T}} \quad \mathbf{f}_g^{\mathrm{T}}\right]^{\mathrm{T}}, \tag{24}$$

where $\mathbf{f}_f$ and $\mathbf{f}_g$ represent the generalized external force vectors acting on the flywheel and frame COMs, respectively.

Then, the generalized external force vector acting on the flywheel COM can be written as:

$$\mathbf{f}_f\Big|_{o_0 x_0 y_0 z_0} = \left[\mathbf{f}_s^{\mathrm{T}} \quad \mathbf{f}_d^{\mathrm{T}}\right]^{\mathrm{T}}. \tag{25}$$

Finally, substituting Eqs. (19) and (22) into Eq. (10), we can obtain vibration equation of the RWA in the time domain. Using small angle hypothesis and ignoring terms with order higher than $O(q_i^2)$, the vibration equation can be written in the following matrix form:

$$\mathbf{M}_R\ddot{\mathbf{q}}_R + (\mathbf{C}_R + \mathbf{G}_R)\dot{\mathbf{q}}_R + \mathbf{K}_R\mathbf{q}_R = \mathbf{p}_R, \tag{26}$$

where $\mathbf{M}_R$, $\mathbf{C}_R$ and $\mathbf{K}_R$ is the generalized mass, damping, and stiffness matrixes of the system, respectively, and $\mathbf{G}_R$ denotes the centrifugal term matrix. All the expressions are shown in follows:

$$\mathbf{M}_R=\begin{bmatrix}\tilde{\mathbf{M}}_f & \mathbf{0}\\ \mathbf{0} & \tilde{\mathbf{M}}_g\end{bmatrix}\ \tilde{\mathbf{M}}_f=\begin{bmatrix}\mathbf{M}_f & \mathbf{0}\\ \mathbf{0} & \mathbf{J}_f\end{bmatrix}\ \tilde{\mathbf{M}}_g=\begin{bmatrix}\mathbf{M}_g & \mathbf{0}\\ \mathbf{0} & \mathbf{J}_g\end{bmatrix}$$
$$\mathbf{K}_R=\begin{bmatrix}\mathbf{K}_0 & -\mathbf{K}_0\\ -\mathbf{K}_0 & \mathbf{K}_0\end{bmatrix}\ \mathbf{C}_R=\begin{bmatrix}\mathbf{C}_0 & -\mathbf{C}_0\\ -\mathbf{C}_0 & \mathbf{C}_0\end{bmatrix}\ \mathbf{G}_R=\begin{bmatrix}\mathbf{G}_f & \mathbf{0}\\ \mathbf{0} & \mathbf{0}\end{bmatrix}, \tag{27}$$

where $\mathbf{G}_f$ is the centrifugal matrix of the flywheel and can be calculated by:

$$\mathbf{G}_f=\begin{bmatrix}\mathbf{0} & \mathbf{0}\\ \mathbf{0} & \mathbf{G}_0\end{bmatrix},\ \mathbf{G}_0=\begin{bmatrix}0 & J_{fz}\Omega & 0\\ -J_{fz}\Omega & 0 & 0\\ 0 & 0 & 0\end{bmatrix}. \tag{28}$$

The generalized coordinate vector of the vibration system is:

$$\mathbf{q}_R\big|_{o_0x_0y_0z_0}=\begin{bmatrix}\mathbf{q}_f^{\mathrm{T}} & \mathbf{q}_g^{\mathrm{T}}\end{bmatrix}^{\mathrm{T}}. \tag{29}$$

RWA WITH A DISCRETE FLEXIBLE STRUCTURE

Description of the Coupling System

Taking a six-dof spring-damping-force of mass system as the discrete structure, vibration characteristics of RWA with the discrete flexible structure are discussed. Simulation parameters of RWA are listed in Table 1. Fig. 6 shows the coupling system and its equivalent model, where d_0 and d_1 are distances from the frame COM and flexible structure to the RWA interface, respectively, and $\mathbf{M}_1$, $\mathbf{C}_1$ and $\mathbf{K}_1$ are mass, damping and stiffness matrixes of the mass system, values of which are defined by:

$$\begin{aligned}\mathbf{M}_1&=\mathrm{diag}\begin{bmatrix}4 & 4 & 4 & 0.006 & 0.006 & 0.01\end{bmatrix},\\ \mathbf{C}_1&=\mathrm{diag}\begin{bmatrix}1000 & 800 & 1200 & 4.5 & 5.8 & 11.5\end{bmatrix},\\ \mathbf{K}_1&=10^5\mathrm{diag}\begin{bmatrix}20 & 10 & 10 & 0.17 & 0.1 & 5.8\end{bmatrix}.\end{aligned} \tag{30}$$

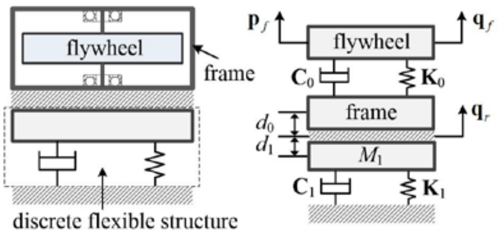

Fig. 6. RWA with a discrete flexible structure.

Model of the Coupling System

Numerical model and FEM of the coupling system are developed in this part. Based on the established vibration equation of RWA, numerical model of RWA with the discrete flexible structure can be obtained as:

$$\mathbf{M}_s\ddot{\mathbf{q}}_s+(\mathbf{C}_s+\mathbf{G}_s)\dot{\mathbf{q}}_s+\mathbf{K}_s\mathbf{q}_s=\mathbf{p}_s, \tag{31}$$

where $\mathbf{M}_s$, $\mathbf{C}_s$, $\mathbf{G}_s$ and $\mathbf{K}_s$ are the mass, damping, centrifugal and stiffness matrixes of the coupling system, respectively, and $\mathbf{q}_s$ and $\mathbf{p}_s$ are the generalized coordinate and external force vectors. All the expressions are shown in follows:

$$\begin{aligned}\mathbf{M}_s&=\begin{bmatrix}\tilde{\mathbf{M}}_f & \mathbf{0}\\ \mathbf{0} & \mathbf{T}_2^{-1}\tilde{\mathbf{M}}_g\mathbf{T}_1+\mathbf{T}_4^{-1}\mathbf{M}_1\mathbf{T}_3\end{bmatrix},\\ \mathbf{K}_s&=\begin{bmatrix}\mathbf{K}_0 & -\mathbf{K}_0\mathbf{T}_1\\ -\mathbf{T}_2^{-1}\mathbf{K}_0 & \mathbf{T}_2^{-1}\mathbf{K}_0\mathbf{T}_1+\mathbf{T}_4^{-1}\mathbf{K}_1\mathbf{T}_3\end{bmatrix},\\ \mathbf{C}_s&=\begin{bmatrix}\mathbf{C}_0 & -\mathbf{C}_0\mathbf{T}_1\\ -\mathbf{T}_2^{-1}\mathbf{C}_0 & \mathbf{T}_2^{-1}\mathbf{C}_0\mathbf{T}_1+\mathbf{T}_4^{-1}\mathbf{C}_1\mathbf{T}_3\end{bmatrix},\\ \mathbf{G}_s&=\begin{bmatrix}\mathbf{G}_f & \mathbf{0}\\ \mathbf{0} & \mathbf{0}\end{bmatrix},\ \mathbf{q}_s=\begin{bmatrix}\mathbf{q}_f^{\mathrm{T}} & \mathbf{q}_r^{\mathrm{T}}\end{bmatrix}^{\mathrm{T}},\end{aligned} \tag{32}$$

where $\mathbf{q}_s$ is the generalized displacement vector of the RWA interface, $\mathbf{T}_1$ and $\mathbf{T}_2$ represent the transitive relations between the displacement and force of the frame COM with the RWA interface, respectively, and $\mathbf{T}_3$ and $\mathbf{T}_4$ represent relations between the flexible structure COM with the RWA interface. They are calculated by:

$$\mathbf{T}_1=\begin{bmatrix}\mathbf{I}_3 & d_0\mathbf{L}\\ \mathbf{0}_3 & \mathbf{I}_3\end{bmatrix},\ \mathbf{T}_2=\begin{bmatrix}\mathbf{I}_3 & \mathbf{0}_3\\ d_0\mathbf{L} & \mathbf{I}_3\end{bmatrix},\ \mathbf{T}_3=\begin{bmatrix}\mathbf{I}_3 & d_1\mathbf{L}^{\mathrm{T}}\\ \mathbf{0}_3 & \mathbf{I}_3\end{bmatrix},$$
$$\mathbf{T}_4=\begin{bmatrix}\mathbf{I}_3 & \mathbf{0}_3\\ d_1\mathbf{L}^{\mathrm{T}} & \mathbf{I}_3\end{bmatrix},\ \mathbf{L}=\begin{bmatrix}0 & 1 & 0\\ -1 & 0 & 0\\ 0 & 0 & 0\end{bmatrix}. \tag{33}$$

Table 1. Simulation parameters of RWA.

Parameters	Values	Parameters	Values
m_f	4.25 kg	k_r	2×10^6 N/m
J_{fr}	0.011 kg·m^2	k_a	8×10^6 N/m
J_{fz}	0.02 kg·m^2	c_r	150 N·s/m
m_b	10 kg	c_a	1000 N·s/m
J_{br}	0.015 kg·m^2	d	0.04 m
J_{bz}	0.03 kg·m^2	d_0	0.055 m
U_s	8.1×10^{-5} kg	d_1	0.005 m
U_d	3.5×10^{-7} kg	φ_s, φ_d	0 rad

ANSYS 13.0 is used to create FEM of the coupling system. In the FEM, element MASS21 is used to mesh the flywheel, frame and mass of the discrete flexible structure, COMBIN14 to mesh the radial and axial equivalent springs of bearings and six-dof spring of the discrete flexible structure, and MPC184 to combine the RWA and mass system.

Modal Analysis of the Coupling System

When the flywheel at rest (Ω=0), based on the numerical model and FEM, first eight orders undamped natural frequencies of the coupling system are obtained and illustrated in Table 2. The results obtained from the numerical model compare well with that from FEM, allowing verification of the numerical model. Only first eight orders natural frequencies are analyzed since the ninth order natural frequency is 273.69 Hz and far greater than the flywheel rotational excitation frequency.

Table 2. Natural frequencies of the coupling system.

Order	1	2	3	4
Numerical (Hz)	34.19	40.14	70.48	70.48
FEM (Hz)	34.19	40.14	70.00	70.48
Order	5	6	7	8
Numerical (Hz)	112.55	116.10	124.41	137.97
FEM (Hz)	112.55	116.10	124.41	137.97

Using the FEM, we can obtain first eight orders mode of vibration, as described in Fig. 7. The first order mode is translational mode of the system along *y*-axis, and second is rock mode about *y*-axis. The third and fourth orders modes are rock modes of the flywheel about *x*-axis and *y*-axis, respectively. The fifth order mode is translational mode of the coupling system along *y*-axis, where the flywheel and frame tend to different directions and involve rock modes. The sixth order model is the translational mode of the flywheel about *x*-axis and rock mode of the frame around *y*-axis. The seventh and eighth order modes are rock mode of the system about *y*-axis and *x*-axis, respectively, where the flywheel and frame rock to different directions.

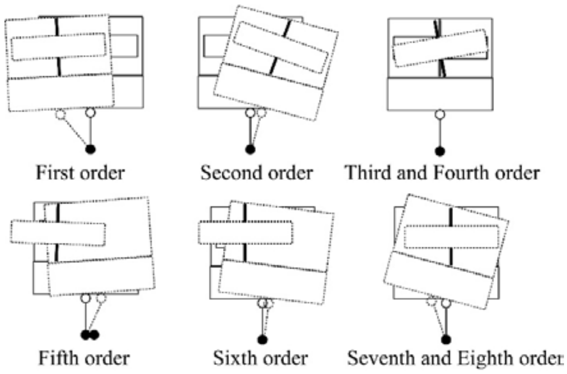

Fig. 7. Modes of vibration of the coupling system.

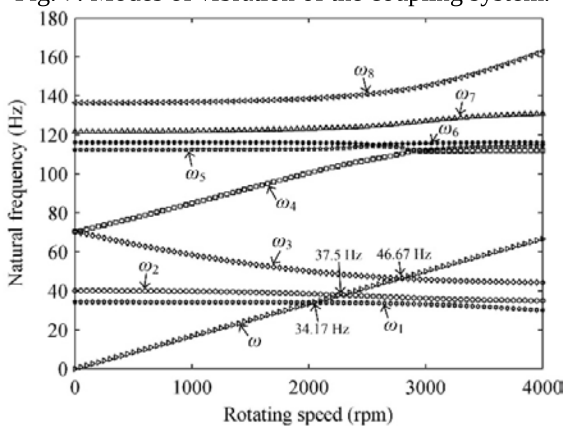

Fig. 8. Campbell diagram of the coupling system.

For a rotating system, the eigenfrequencies often depend on the rotational speed as a result of the gyroscopic effect. The variation of the eigenfrequencies with the rotational speed is often plotted in a diagram called a Campbell diagram. Fig. 8 shows Campbell diagram of the coupling system, which plots the variation of the first eight order undamped natural frequencies with the flywheel rotating speed, and eight curves are defined as ω_i (i=1, 2…8) corresponding to the *i*th order natural frequency. In addition, the dotted line refers the excitation frequency of the flywheel imbalance.

It can be seen from Fig. 8 that there is a pair of backward and forward whirl curves, ω_3 and ω_4, ω_3 is the backward whirl curves, decreasing with the speed of the flywheel, and ω_4 is the forward whirl curves, increasing with the flywheel rotation speed, very close to the translational mode of the coupling system, ω_5, when the rotational speed is higher than 2800 rpm. The other six natural frequencies basically remain unchanged at low rotational speed and would change when the rotational speeds are higher than 2000 rpm. These changes are no more than 5 Hz, except ω_7 and ω_8 beyond 10 Hz.

The spin speeds at which one of the excitation functions has a frequency coinciding with one of the natural frequencies of the system are usually referred to a critical speed (Genta et al., 2005). In the coupling system, the excitation frequency of the flywheel imbalance is $\omega=\Omega/60$. Thus, as labeled in Fig. 8, there are three critical speeds in the coupling system, which nearly locate at 2050 rpm, 2250 rpm and 2800 rpm corresponding to excitation frequency are 34.17Hz, 37.5Hz and 46.67Hz, respectively. At these critical speeds, the flywheel imbalance can trigger dynamic amplification of amplitude, and the system will experience large vibrations.

Dynamic Response Analysis of the RWA Interface

Assuming initial condition is $\dot{\mathbf{q}}_s = \mathbf{q}_s = \mathbf{0}$ and taking the Laplace transform to Eq. (31), we can obtain that:

$$\begin{bmatrix} \mathbf{A} & \mathbf{B} \\ \mathbf{C} & \mathbf{D} \end{bmatrix} \begin{bmatrix} \mathbf{X}_f \\ \mathbf{X}_r \end{bmatrix} = \begin{bmatrix} \mathbf{F}_f \\ \mathbf{0} \end{bmatrix},$$

$$\begin{aligned} &\mathbf{A} = \tilde{\mathbf{M}}_f s^2 + (\mathbf{G}_f + \mathbf{C}_0)s + \mathbf{K}_0, \\ &\mathbf{B} = -(\mathbf{C}_0 s + \mathbf{K}_0)\mathbf{T}_1, \\ &\mathbf{C} = -\mathbf{T}_2^{-1}(\mathbf{C}_0 s + \mathbf{K}_0), \\ &\mathbf{D} = \mathbf{T}_2^{-1}(\tilde{\mathbf{M}}_g s^2 + \mathbf{C}_0 s + \mathbf{K}_0)\mathbf{T}_1 + \\ &\quad \mathbf{T}_4^{-1}(\mathbf{M}_1 s^2 + \mathbf{C}_1 s + \mathbf{K}_1)\mathbf{T}_3, \end{aligned} \tag{34}$$

where $s=wi=2\pi fi$, i is the square root of –1, w and f are vibration angular frequency and vibration frequency, respectively, and vectors $\mathbf{X}_f$, $\mathbf{X}_r$, and $\mathbf{F}_f$ are frequency domain form expressions of the generalized displacement vectors.

The generalized external force vector in the frequency domain form can be expressed as:

$$\mathbf{F}_f = \begin{bmatrix} U_s w^2 & U_s w^2 i & 0 & U_d w^2 & U_d w^2 i & 0 \end{bmatrix}^{\mathrm{T}}. \quad (35)$$

Then, acceleration response of the RWA interface can be obtained as:

$$\ddot{\mathbf{X}}_r = (\mathbf{B} - \mathbf{A}\mathbf{C}^{-1}\mathbf{D})\mathbf{F}_f s^2. \quad (36)$$

Matlab R2017a and ANSYS 13.0 are used to simulate acceleration response of the RWA interface via the numerical model in Eq. (36) and the established FEM of the RWA, respectively. The numerical simulations are performed when the flywheel rotating speed is stabilizing at Ω=1, 2…4000 rpm. Acting unbalance force and moment to the MASS element of the flywheel, the FEM simulations are performed when the flywheel rotating speed is stabilizing at Ω=(2l–1)·60 rpm (l=1, 2…34).

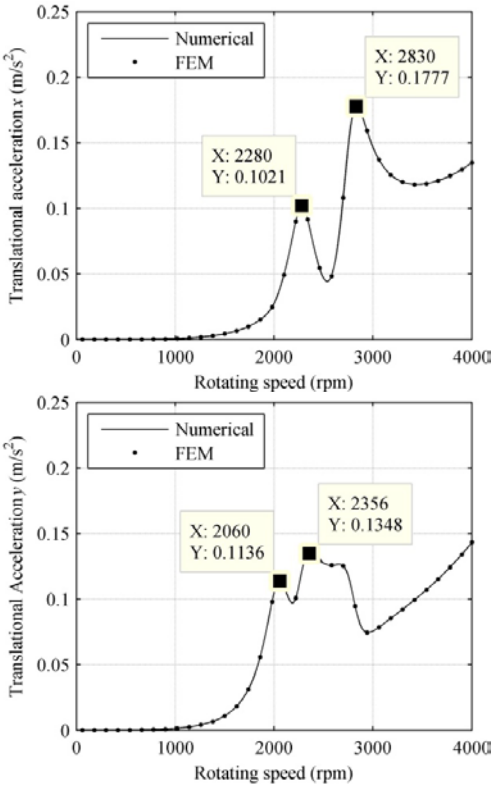

Fig. 9. Comparison result of translational acceleration.

Figs. 9 and 10 plot the translational and angular acceleration amplitudes of the two simulations at the fundamental frequency, respectively. It can be seen from the figures that the two simulation results are basically consistent, which further validates the numerical model. The acceleration response can trigger obvious amplitude amplification at the critical speed as discussed in last part, but the critical speed points have small difference with the Campbell diagram because influence of the damping. The first critical speed is intersection of the excitation frequency with the first order mode (translational mode of the system along y-axis) and triggers amplification of translational acceleration amplitude along y-axis near 2040 rpm. Similarly, the second critical speed triggers amplification of translational acceleration amplitude along x-axis near 2280 rpm. Since the height difference between the flywheel imbalance excitations with the RWA interface, force excitations of the flywheel along x-axis and y-axis can bring moments about y-axis and x-axis, respectively. Hence, the first and second critical speeds also trigger amplification of angular acceleration amplitudes about x-axis near 2040 rpm and y-axis near 2280 rpm, respectively. The third critical speed is the backward whirl curves with the excitation frequency and can excite amplification of translational acceleration amplitude along x-axis and angular acceleration amplitude about x-axis and y-axis near 2830 rpm.

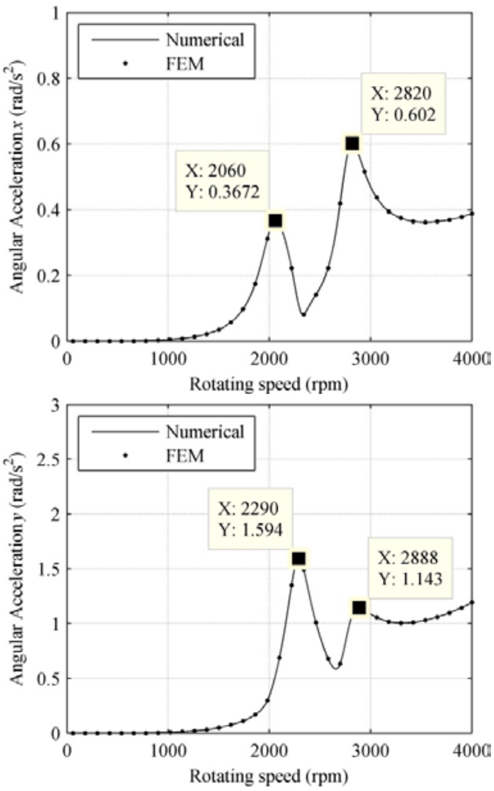

Fig. 10. Comparison result of angular acceleration.

RWA WITH A CONTINUOUS FLEXIBLE STRUCTURE

Frequency Domain Substructure Method

A FDSM is used to develop the coupling analysis model. Early FDSM is the Impedance Coupling method (IC method), which uses receptance of substructures to obtain that of the assembly structure (Imregun et al., 1987). However, this method is computationally inefficient since it needs to inverse the receptance of each substructure firstly. Tsai and Chou et al. (1988) developed a Receptance Coupling method (RC method), which is more computational efficiency by synthesizing receptance of substructures directly and will be adopt by this paper.

Taking coupling process of two substructures as example, the RC method is deduced, as described in Fig. 11. Subscripts a and b represent internal coordinates on the two substructures, respectively, and c represent the connection coordinates. Defining coordinate $o_1x_1y_1z_1$ (coordinate 1) and coordinate $o_2x_2y_2z_2$ (coordinate 2) are their local coordinates.

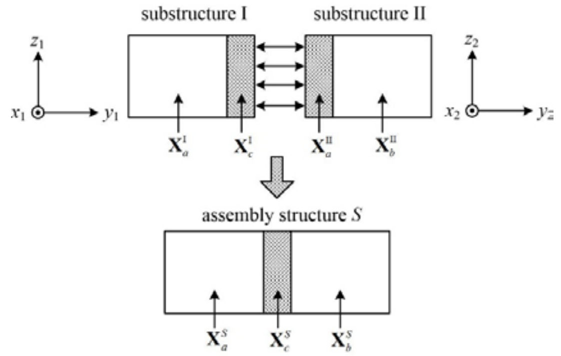

Fig. 11. Coupling process of two substructures.

Defining receptance matrixes of assembly structure S, substructures I and II in partitioned form as follows:

$$\mathbf{H}^S=\begin{bmatrix}\mathbf{H}^S_{aa} & \mathbf{H}^S_{ac} & \mathbf{H}^S_{ab}\\ \mathbf{H}^S_{ca} & \mathbf{H}^S_{cc} & \mathbf{H}^S_{cb}\\ \mathbf{H}^S_{ba} & \mathbf{H}^S_{bc} & \mathbf{H}^S_{bb}\end{bmatrix},\ \begin{Bmatrix}\mathbf{X}^S_a\\ \mathbf{X}^S_c\\ \mathbf{X}^S_b\end{Bmatrix}=\mathbf{H}^S\begin{Bmatrix}\mathbf{F}^S_a\\ \mathbf{F}^S_c\\ \mathbf{F}^S_b\end{Bmatrix}, \tag{37}$$

$$\mathbf{H}^{\mathrm{I}}=\begin{bmatrix}\mathbf{H}^{\mathrm{I}}_{aa} & \mathbf{H}^{\mathrm{I}}_{ac}\\ \mathbf{H}^{\mathrm{I}}_{ca} & \mathbf{H}^{\mathrm{I}}_{cc}\end{bmatrix},\ \begin{Bmatrix}\mathbf{X}^{\mathrm{I}}_a\\ \mathbf{X}^{\mathrm{I}}_c\end{Bmatrix}=\mathbf{H}^{\mathrm{I}}\begin{Bmatrix}\mathbf{F}^{\mathrm{I}}_a\\ \mathbf{F}^{\mathrm{I}}_c\end{Bmatrix}, \tag{38}$$

$$\mathbf{H}^{\mathrm{II}}=\begin{bmatrix}\mathbf{H}^{\mathrm{II}}_{bb} & \mathbf{H}^{\mathrm{II}}_{bc}\\ \mathbf{H}^{\mathrm{II}}_{cb} & \mathbf{H}^{\mathrm{II}}_{cc}\end{bmatrix},\ \begin{Bmatrix}\mathbf{X}^{\mathrm{II}}_b\\ \mathbf{X}^{\mathrm{II}}_c\end{Bmatrix}=\mathbf{H}^{\mathrm{II}}\begin{Bmatrix}\mathbf{F}^{\mathrm{II}}_b\\ \mathbf{F}^{\mathrm{II}}_c\end{Bmatrix}, \tag{39}$$

where $\mathbf{H}$ represents receptance matrix, and $\mathbf{X}$ and $\mathbf{F}$ refer to response and excitation vectors, respectively.

When coordinates 1 and 2 are inconsistent, they need been transformed into accordant. After the transformation, assuming coordinate 2 accordance to coordinate 1, all the coordinates of substructure II need to be transformed by a coordinate transformation matrix, which is defined as:

$$\mathbf{T}^{\mathrm{II}}=\begin{bmatrix}\mathbf{T}_b & \mathbf{0}\\ \mathbf{0} & \mathbf{T}_c\end{bmatrix}, \tag{40}$$

where $\mathbf{T}_b$ and $\mathbf{T}_c$ are the orientation cosine matrixes between internal and connection coordinates of substructure II with that of substructure I, respectively.

After been transformed, Eq. (39) can be rewritten as:

$$\tilde{\mathbf{H}}^{\mathrm{II}}=\begin{bmatrix}\mathbf{T}_b^{-1}\mathbf{H}^{\mathrm{II}}_{bb}\mathbf{T}_b & \mathbf{T}_b^{-1}\mathbf{H}^{\mathrm{II}}_{bc}\mathbf{T}_c\\ \mathbf{T}_c^{-1}\mathbf{H}^{\mathrm{II}}_{cb}\mathbf{T}_b & \mathbf{T}_c^{-1}\mathbf{H}^{\mathrm{II}}_{cc}\mathbf{T}_c\end{bmatrix},\ \begin{Bmatrix}\tilde{\mathbf{X}}^{\mathrm{II}}_b\\ \tilde{\mathbf{X}}^{\mathrm{II}}_c\end{Bmatrix}=\tilde{\mathbf{H}}^{\mathrm{II}}\begin{Bmatrix}\tilde{\mathbf{F}}^{\mathrm{II}}_b\\ \tilde{\mathbf{F}}^{\mathrm{II}}_c\end{Bmatrix}, \tag{41}$$

where $\tilde{\mathbf{X}}^{\mathrm{II}}$ and $\tilde{\mathbf{F}}^{\mathrm{II}}$ refer to excitation and response vectors of substructure I on coordinate 1, respectively, and $\tilde{\mathbf{H}}^{\mathrm{II}}$ represents the receptance matrix.

Basic conditions of the substructures synthesis are compatibility and equilibrium of the connection coordinates, which are given as:

$$\mathbf{X}^{\mathrm{I}}_c=\tilde{\mathbf{X}}^{\mathrm{II}}_c=\mathbf{X}^S_c,\ \mathbf{F}^{\mathrm{I}}_c+\tilde{\mathbf{F}}^{\mathrm{II}}_c=\mathbf{F}^S_c. \tag{42}$$

In the substructures coupling process, response and excitation of the internal coordinates are not changed, which can be expressed by:

$$\mathbf{X}^{\mathrm{I}}_a=\mathbf{X}^S_a,\ \tilde{\mathbf{X}}^{\mathrm{II}}_b=\mathbf{X}^S_b,\ \mathbf{F}^{\mathrm{I}}_a=\mathbf{F}^S_a,\ \tilde{\mathbf{F}}^{\mathrm{II}}_b=\mathbf{F}^S_b. \tag{43}$$

Combining Eqs. (37)–(43), we can obtain expression of receptance matrix of the assembly structure:

$$\mathbf{H}^S=\begin{bmatrix}\mathbf{H}^{\mathrm{I}}_{aa} & \mathbf{H}^{\mathrm{I}}_{ac} & \mathbf{0}\\ \mathbf{H}^{\mathrm{I}}_{ca} & \mathbf{H}^{\mathrm{I}}_{cc} & \mathbf{0}\\ \mathbf{0} & \mathbf{0} & \mathbf{T}_b^{-1}\mathbf{H}^{\mathrm{II}}_{bb}\mathbf{T}_b\end{bmatrix}-\begin{bmatrix}\mathbf{H}^{\mathrm{I}}_{ac}\\ \mathbf{H}^{\mathrm{I}}_{cc}\\ -\mathbf{T}_b^{-1}\mathbf{H}^{\mathrm{II}}_{bc}\mathbf{T}_c\end{bmatrix} \left[\mathbf{H}^{\mathrm{I}}_{cc}+\mathbf{T}_c^{-1}\mathbf{H}^{\mathrm{II}}_{cc}\mathbf{T}_c\right]^{-1}\begin{bmatrix}\mathbf{H}^{\mathrm{I}}_{ca}\\ \mathbf{H}^{\mathrm{I}}_{cc}\\ -\mathbf{T}_c^{-1}\mathbf{H}^{\mathrm{II}}_{cb}\mathbf{T}_b\end{bmatrix}^{\mathrm{T}}. \tag{44}$$

RC method can be used to structure receptance matrix of the coupling system by taking impedance matrixes of RWA and flexible structure into Eq. (44). The whole process requires only inversion of impedance matrix of the connection coordinates, making improvement of the calculation accuracy and efficiency. Steps involved in the coupling process can be summarized as follows:

1) Dividing the coupling system into RWA and flexible structure substructures;

2) Calculating impedance matrixes of the RWA and flexible structure and the coordinate transformation matrix;

3) Achieving receptance matrix of the coupling system by substituting the obtained impedance matrixes and coordinate transformation matrix into Eq. (44).

Division of Substructures

Taking an aluminum honeycomb sandwich palate (AHSP) as the continuous flexible structure, coupling system of RWA with a continuous flexible structure is shown in Fig. 12, where RWA is mounted on the central of the aluminum honeycomb sandwich palate with 45º angle of inclination about y-axis.

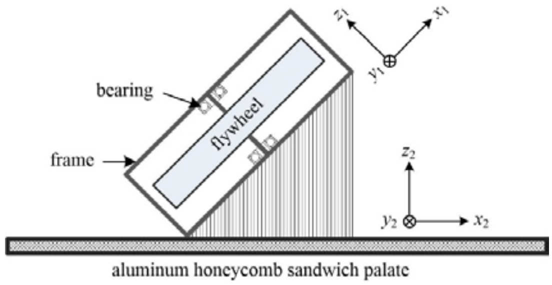

Fig. 12. Coupling system of RWA with an AHSP.

The coupling system can be divided into RWA substructure (substructure I) and flexible structure substructure (substructure II).

Substructure I

Receptance matrix of substructure I can be obtained by the vibration equation of RWA. Internal coordinates of substructure I are the flywheel COM, and connection coordinates are the RWA interface. Vibration equation of the RWA based on the internal and connection coordinates can be expressed as:

$$\begin{bmatrix}\tilde{\mathbf{M}}_f & \mathbf{0}\\ \mathbf{0} & \mathbf{T}_2^{-1}\tilde{\mathbf{M}}_g\mathbf{T}_1\end{bmatrix}\begin{Bmatrix}\ddot{\mathbf{q}}_f\\ \ddot{\mathbf{q}}_r\end{Bmatrix}+\begin{bmatrix}\mathbf{G}_f+\mathbf{C}_0 & -\mathbf{C}_0\mathbf{T}_1\\ -\mathbf{T}_2^{-1}\mathbf{C}_0 & \mathbf{T}_2^{-1}\mathbf{C}_0\mathbf{T}_1\end{bmatrix}\begin{Bmatrix}\dot{\mathbf{q}}_f\\ \dot{\mathbf{q}}_r\end{Bmatrix}+ \begin{bmatrix}\mathbf{K}_0 & -\mathbf{K}_0\mathbf{T}_1\\ -\mathbf{T}_2^{-1}\mathbf{K}_0 & \mathbf{T}_2^{-1}\mathbf{K}_0\mathbf{T}_1\end{bmatrix}\begin{Bmatrix}\mathbf{q}_f\\ \mathbf{q}_r\end{Bmatrix}=\begin{Bmatrix}\mathbf{p}_f\\ \mathbf{p}_r\end{Bmatrix}. \tag{45}$$

Using Eq. (45), we can obtain receptance matrix of substructure I:

$$\mathbf{H}^{\mathrm{I}}=\begin{bmatrix}\mathbf{H}_{aa}^{\mathrm{I}} & \mathbf{H}_{ac}^{\mathrm{I}}\\ \mathbf{H}_{ca}^{\mathrm{I}} & \mathbf{H}_{cc}^{\mathrm{I}}\end{bmatrix}= \begin{bmatrix}\tilde{\mathbf{M}}_f s^2+(\mathbf{C}_0+\mathbf{G}_f)s+\mathbf{K}_0 & -(\mathbf{K}_0+\mathbf{C}_0 s)\mathbf{T}_1\\ -\mathbf{T}_2^{-1}(\mathbf{K}_0+\mathbf{C}_0 s) & \mathbf{T}_2^{-1}(\tilde{\mathbf{M}}_g s^2+\mathbf{C}_0 s+\mathbf{K}_0)\mathbf{T}_1\end{bmatrix}^{-1}. \tag{46}$$

Substructure II

Substructure II only takes connection coordinate of the RWA interface into account. Receptance matrix of substructure II will be calculated using FEM of the AHSP.

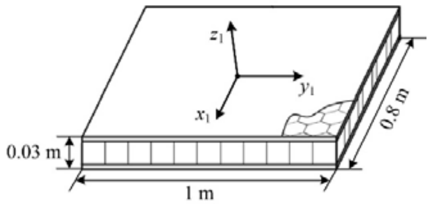

Fig. 13. Schematic diagram of the AHSP.

As described in Fig. 13, the AHSP structure is made of two layers of aluminum skins on the two sides with hexagon honeycombs core in the middle. The AHSP can be regarded as a laminate with three layers palate since the honeycombs core can be equivalent into homogeneous orthotropic material. The thickness of single layer aluminum skin is 0.3 mm. Material properties of the aluminum skins and honeycombs core equivalent model are listed in Tables 3 and 4, respectively, which are derived from Sun et al. (2017), where E, G, ρ and υ are Young's module, shear module, density and Poisson ratio, respectively.

Table 3. Material properties of aluminum alloy.

Young's modules (E)	Density (ρ)	Poisson Ratio (υ)
71 GPa	2700 kg/m^3	0.33

Table 4. Equivalent properties of honeycombs core.

Properties	Value	Properties	Value
E_{xx}	0.0354 MPa	G_{zx}	92.463 MPa
E_{yy}	0.0354 MPa	ρ	24.94 kg/m^3
E_{zz}	655.87 MPa	υ_{12}	0.999856
G_{xy}	0.0266 MPa	υ_{23}	0
G_{yz}	141.12 MPa	υ_{31}	0

ANSYS 13.0 is used to establish FEM of the AHSP. In the FEM, element SHELL181 is applied to mesh the AHSP and the shell section is made of three layers of planes, nodes at four corners are fixed, and structural damping ratio is set as 0.01. Employing harmonic response analysis to the FEM, receptance matrix of substructure II can be obtained by acting six-dof unit force to the RWA interface independent.

Dynamic Response of the Coupling System

Connection coordinates of substructure II need to be transformed, and the coordinate transformation matrix is given as:

$$\mathbf{T}_c=\begin{bmatrix}\mathbf{T}_{c1} & \mathbf{0}\\ \mathbf{0} & \mathbf{T}_{c1}\end{bmatrix},\ \mathbf{T}_{c1}=\begin{bmatrix}\cos\theta & 0 & \sin\theta\\ 0 & 1 & 0\\ -\sin\theta & 0 & \cos\theta\end{bmatrix}. \tag{47}$$

Thus, receptance matrix of the coupling system is achieved by taking the receptance matrix of substructure II, Eqs. (46) and (47) into Eq. (44), which is expressed as:

$$\mathbf{H}^S=\mathbf{H}^{\mathrm{I}}-\begin{bmatrix}\mathbf{H}_{ac}^{\mathrm{I}}\\ \mathbf{H}_{cc}^{\mathrm{I}}\end{bmatrix}\left[\mathbf{H}_{cc}^{\mathrm{I}}+\mathbf{T}_c^{-1}\mathbf{H}_{cc}^{\mathrm{II}}\mathbf{T}_c\right]^{-1}\begin{bmatrix}\mathbf{H}_{ca}^{\mathrm{I}}\\ \mathbf{H}_{cc}^{\mathrm{I}}\end{bmatrix}^{\mathrm{T}}. \tag{48}$$

For the coupling system, only external excitation acts on the flywheel. The external excitation vector of the coupling system can be written as:

$$\mathbf{F}_S=\left[\mathbf{F}_f^{\mathrm{T}}\quad \mathbf{0}^{\mathrm{T}}\right]^{\mathrm{T}}. \tag{49}$$

Multiplying receptance matrix of the coupling system by the external excitation vector, we can obtain the displacement responses, by which the acceleration responses are achieved:

$$\ddot{\mathbf{X}}_S=\mathbf{H}^S\mathbf{F}_S s^2. \tag{50}$$

Simulation and Verification

To validate the acceleration responses obtained by the RC method, Matlab R2017a and ANSYS 13.0 are used to perform numerical and FEM simulations of the coupling system. The numerical simulations are conduct by using Eq.(50), when the flywheel rotating speed is stabilizing at $\Omega=l$ rpm (l=1, 2…4000). Based on the FEMs of the RWA and AHSP established on the previous, FEM of the coupling system is established. The FEM simulations are performed when the flywheel rotating speed is stabilizing at $\Omega=(2l-1)\cdot 60$ rpm (l=1, 2…34).

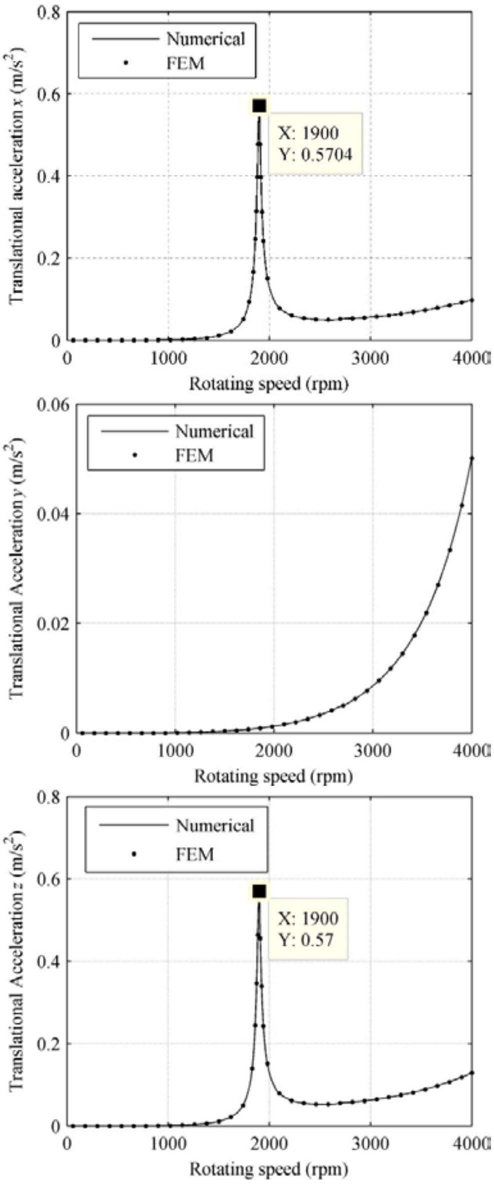

Fig. 14. Comparison result of translational acceleration.

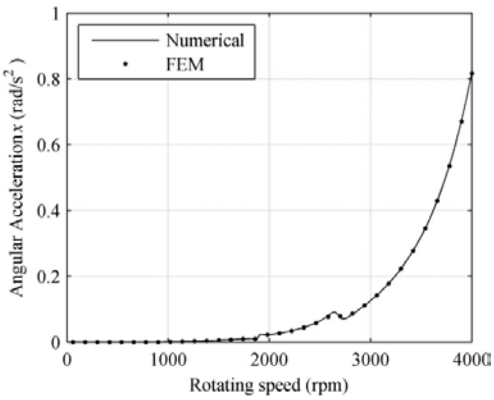

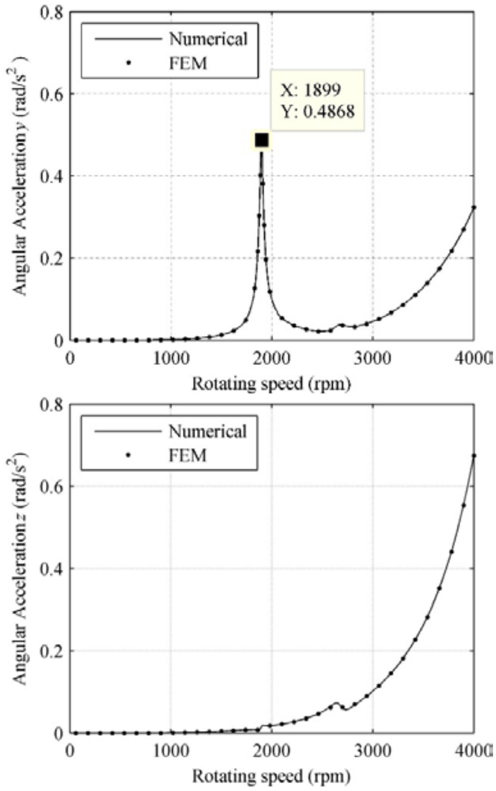

Fig. 15. Comparison result of angular acceleration.

Simulation results of translational and angular acceleration responses of the two simulations at the fundamental frequency are shown in Figs. 14 and 15, respectively. What can be obtained from the figures that the two simulation results are basically consistently. The simulation errors of the dynamic response by the RC method are within plus-minus five percent. The results turn out that the RC method can accurately predict the coupled micro-vibrations of RWA with the flexible structure. In addition, similar to the discrete flexible structure, the acceleration response of RWA with the continuous flexible structure also would trigger obvious amplitude amplification at the critical speed, which in this situation occurs nearly 1900 rpm.

CONCLUSIONS

In this paper, the coupled micro-vibrations between a RWA with both a discrete and continuous flexible structures are discussed. At first, the RWA model is simplified into a twelve-dof linear vibration system with gyroscopic term, where the flywheel and frame are considered as six-dof rigid bodies, and the bearings are equivalent to a six-dof spring with stiffness and damping. The generalized external force vector acting on the flywheel is caused by the flywheel static and dynamic mass imbalances. The Lagrange's energy method is used to develop its vibration equation. Then, based on the established vibration equation, disturbance model of the RWA with a six-dof discrete flexible structure is developed. Vibration characteristics of the coupling system are simulated and analyzed by numerical and FEM simulations. The results illustrate that natural frequencies of the coupling system are changed with the flywheel rotational speeds, especially for a pair of backward and forward whirl curves, and the system contains three critical speeds, at which the flywheel imbalance will trigger dynamic amplification of amplitude and the system could experience large amplitude vibrations. Last but not least, a coupling system of the RWA with a continuous flexible structure is studied based on the RC method. The coupling system is divided into RWA and flexible structure substructures, and the RC method is used to calculate its disturbance response. Numerical and FEM simulations performed to validate this dynamic response are presented with encouraging results: predictions of dynamic responses achieved by the RC method consistently predicted the results of the FEM simulation with the simulation error less than five percent. Therefore, the RC method can be used to predict micro-vibrations characteristics of the RWA-flexible structure coupling system with high prediction accuracy and computational efficiency. In conclusion, on the basis of all the conclusions drawn from this paper, this paper will provide a theoretical basis for prediction of the coupled disturbance of RWA on the satellite flexible installation interface.

REFERENCES

Remedia, M., Aglietti, G. S., Richardson, G., et al., “Integrated Semiempirical Methodology for Micro-vibration Prediction,” AIAA Journal, Vol. 53, pp. 1236-1250, (2015).

Chen, J. and Cheng, W., “Research on the disturbance generated by a solar array drive assembly driving a flexible system,” Journal of Theoretical & Applied Mechanics, Vol. 54, pp. 1001-1012, (2016).

Li, X. F., Cheng W. and Li, M., “Testing and Analysis of Micro-vibrations Generated by Control Moment Gyroscope in Different Installation Boundary,” Applied Mechanics and Materials, Vol. 851, pp. 453-458, (2016).

Zhang, P. F., Cheng, W., Wang, H., et al., “Disturbance modeling and parameters identification of reaction wheel assembly on spacecraft,” Journal of Beijing University of Aeronautics and Astronautics, Vol. 36, pp. 879-882, (2010).

Li, X., Cheng, W. and Li, X. F., “Modelling of Frame Control Moment Gyro and Analysis of Frame Disturbance Impact,” Tehnicki Vjesnik, Vol. 21, pp. 1189-1199, (2014).

Masterson, R. A., Miller D. W. and Grogan, R. L., “Development and validation of reaction wheel disturbance models: Empirical model,” Journal of Sound and Vibration, Vol. 249, pp. 575-598, (2002).

Masterson, R. A., “Development and validation of empirical and analytical reaction wheel disturbance models,” Dissertation for the Master Degree in Massachusetts Institute of Technology, Massachusetts, USA, (1999).

Narayan, S. S., Nair, P. S. and Ghosal, A., “Dynamic interaction of rotating momentum wheels with spacecraft elements,” Journal of Sound and Vibration, Vol. 315, pp. 970-984, (2008).

Elias, L. M., Dekens, F. G., Basdogan, I., et al., “A methodology for modeling the mechanical interaction between a reaction wheel and a flexible structure,” Proceedings of SPIE, Hawaii, USA, Vol. 4852, pp. 541-555, (2003).

Elias, L. M., “A structurally coupled disturbance analysis method using dynamic mass measurement techniques, with application to spacecraft reaction wheel systems,” Dissertation for the Master Degree in Massachusetts Institute of Technology, Massachusetts, USA, (1999).

Elias, L. and Miller, D., “A Coupled Disturbance Analysis Method Using Dynamic Mass Measurement Techniques,” Proceedings of the 43rd AIAA/ASME/ASCE/AHS/ASC Structures, Structural Dynamics, and Materials Conference, Denver, April, Vol. 1252, pp. 1-12, (2002).

Zhou, W. Y., Aglietti, G. S. and Zhang, Z., “Modelling and testing of a soft suspension design for a reaction/momentum wheel assembly,” Journal of Sound and Vibration, Vol. 330, pp. 4596-4610, (2011).

Zhang, Z., Aglietti, G. S. and Ren, W., “Coupled microvibration analysis of a reaction wheel assembly including gyroscopic effects in its accelerance,” Journal of Sound and Vibration, Vol. 332, pp. 5748-5765, (2013).

Zhou, W., LI, D., Luo, Q., et al., “Analysis and Testing of Microvibrations Produced by Momentum Wheel Assemblies,” Chinese Journal of Aeronautics, Vol. 25, pp. 640-649, (2012).

Chen, S., Q., Introduction of Analytical Mechanics, Tongji University Press, Shanghai, (1997).

Yuan, H., Q., Rotor Dynamics, Metallurgy Industry Press, Beijing, (2013).

Genta, G., Dynamics of Rotating Systems, Springer US, USA, (2005).

Imregun, M., Robb, D. A. and Ewins, D. J., “Structural modification and coupling dynamic analysis using measured FRF data,” Proceedings of the 5th International Modal Analysis Conference, London, England, pp. 1136-1141(1987).

Tsai, J. S. and Chou, Y. F., "The identification of dynamic characteristics of a single bolt connection," Journal of Sound and Vibration, Vol. 125, pp. 487-502, (1988).

Sun, W. Q. and Cheng, W., "Finite element model updating of honeycomb sandwich plates using a response surface model and global optimization technique," Structural and Multidisciplinary Optimization, Vol. 55, pp. 121-139, (2017).

NOMENCLATURE

m	mass
J	inertia
k	stiffness
c	damping
F	force
T	torque
d	bearings supporting length
d_0	distance between COMs of the frame and RWA interface
d_1	distance between COMs of the flexible structure and RWA interface
q	generalized coordinate
p	generalized external force
T	kinetic energy
V	potential energy
D	dissipations energy
Ω	flywheel spinning speed
f_s	static imbalance force of the flywheel
f_d	dynamic imbalance torque of the flywheel
ω	excitation frequency of the flywheel imbalance
$\mathbf{G}$	centrifugal term matrix
$\mathbf{H}$	receptance matrix
$\mathbf{X}$	response vector
$\mathbf{F}$	excitation vector
$\mathbf{T}$	orientation cosine matrix
E	Young's module
G	shear module
ρ	density
υ	Poisson ratio

Subscripts

f	the flywheel
g	the frame
t	translational direction
r	radial direction
R	vibration system of the RWA
s	vibration system of the RWA with discrete flexible structure
a,b	internal coordinates on two substructures
c	connection coordinates on two substructures

Superscript

S	assembly structure
I	substructure I
II	substructure II

動量輪與彈性結構的耦合微振動特性研究

李雄飛　　程偉

北京航空航天大學航空科學與工程學院

摘 要

本文主要研究動量輪與彈性結構的耦合微振動特性。首先，將動量輪模型簡化爲考慮陀螺效應的12自由度線性微分方程，並採用Lagrange能量方法建立其振動方程；其次，基於該振動方程建立動量輪與離散彈性結構的耦合振動方程，並選取一個6自由度系統作爲離散彈性結構，仿真分析了耦合系統的振動特性；再次，應用頻域子結構法方法推導動量輪與連續彈性結構的耦合振動響應，並運用數值仿真和有限仿真進行了驗證，該方法可以用於計算動量輪與衛星彈性安裝界面的振動響應。本文提出的耦合振動分析方法可爲預測動量輪與衛星彈性安裝界面的微振動響應提供理論基礎。